MOLECULAR NEUROSCIENCE

10.1126/sciadv.1600014

Copper-induced structural conversion templates prion protein oligomerization and neurotoxicity

Chi-Fu Yen,[1] Dilshan S. Harischandra,[2] Anumantha Kanthasamy,[2] Sanjeevi Sivasankar[1,3]*

Prion protein (PrP) misfolding and oligomerization are key pathogenic events in prion disease. Copper exposure has been linked to prion pathogenesis; however, its mechanistic basis is unknown. We resolve, with single-molecule precision, the molecular mechanism of Cu^{2+}-induced misfolding of PrP under physiological conditions. We also demonstrate that misfolded PrPs serve as seeds for templated formation of aggregates, which mediate inflammation and degeneration of neuronal tissue. Using a single-molecule fluorescence assay, we demonstrate that Cu^{2+} induces PrP monomers to misfold before oligomer assembly; the disordered amino-terminal region mediates this structural change. Single-molecule force spectroscopy measurements show that the misfolded monomers have a 900-fold higher binding affinity compared to the native isoform, which promotes their oligomerization. Real-time quaking-induced conversion demonstrates that misfolded PrPs serve as seeds that template amyloid formation. Finally, organotypic slice cultures show that misfolded PrPs mediate inflammation and degeneration of neuronal tissue. Our study establishes a direct link, at the molecular level, between copper exposure and PrP neurotoxicity.

INTRODUCTION

Protein misfolding and oligomeric protein accumulation are key pathogenic mechanisms in many major neurodegenerative disorders, including prion diseases, Parkinson's disease, and Alzheimer's disease (*1*). Propagation of protein misfolding in these disorders is believed to proceed through a common prion-like mechanism, which means that proteins misfold, impose their structures on natively folded proteins, and template their aggregation (*2*). Although the structure of natively folded prion protein (PrP) has been resolved (*3*–*6*), the mechanistic basis for its misfolding, aggregation, and neurotoxicity is unknown.

PrP is a metal-binding protein; the unstructured N-terminal tail of PrP contains four copies of an octarepeat sequence, which bind a number of divalent ions, including Cu^{2+}, Ni^{2+}, and Mn^{2+} (Fig. 1A) (*7*–*9*). Metal ions also bind to an additional site in the flexible region between the octarepeats and the C-terminal domain (*10*). It has been proposed that Cu^{2+} ions play a role in PrP structural conversion (*11*); however, direct molecular proof for the role of Cu^{2+} in PrP misfolding and aggregation is lacking. Biochemical experiments show that PrPs incubated with Cu^{2+} ions misfold from a native, α helix–rich structure to a predominantly β sheet conformation that is resistant to proteolytic digestion (*12*, *13*). Along the same lines, aggregation of PrP is enhanced either by the insertion of additional octapeptide repeats or by exposure to high concentrations of Cu^{2+} (*14*, *15*). However, the mechanisms by which Cu^{2+} induces PrP misfolding, aggregation, and neurotoxicity are unknown.

Here, we resolve, with single-molecule precision, Cu^{2+}-induced misfolding of PrP under physiological conditions. We also demonstrate that the misfolded PrPs serve as seeds for the templated formation of aggregates, which mediate inflammation and degeneration of neuronal tissue. We compare the biophysical properties of full-length, human PrP with globular protein lacking the N-terminal octapeptide repeats in the presence and absence of Cu^{2+}, Ni^{2+}, and Mn^{2+} (Fig. 1). Using a fluorescence-based single-molecule assay, we demonstrate that PrP monomers misfold to a protease-resistant conformation before oligomer assembly; the N-terminal region and Cu^{2+} ions mediate misfolding. This is a striking result because the conventional model is that protease resistance is acquired only by oligomers; in fact, protease resistance is often used as a readout for PrP oligomerization (*16*). Using single-molecule force measurements with an atomic force microscope (AFM), we show that misfolded PrP monomers have an almost 900-fold higher affinity (K_A) compared to the native isoform and rapidly form oligomers. Using real-time quaking-induced conversion (RT-QuIC) (*17*), which is a cell-free seeding assay designed for rapid clinical diagnosis of prion disease, we show that misfolded PrPs form active seeds that template aggregation. Finally, to investigate the effect of Cu^{2+}-induced PrP misfolding on neuronal viability, we quantify protein markers for inflammation, apoptosis, and oxidative stress in brain explants exposed to native and misfolded PrPs. Analysis of these organotypic slice cultures provides direct molecular proof that the misfolded PrPs mediate neuroinflammation and neurodegeneration. Together, our results identify conditions for Cu^{2+}-induced PrP misfolding, oligomerization, and neurotoxicity.

RESULTS

N-terminal region and Cu^{2+} ions mediate protease resistance in PrP monomers

A common characteristic of PrP misfolding is the conversion of native, proteinase K (PK)–sensitive PrP (PrP^{sen}) into an isoform that is prone to aggregation and resists PK digestion (PrP^{res}) (*18*–*20*). To identify misfolded PrPs and determine the role of different metal ligands and of the N- and C-terminal domains in PrP misfolding, we developed a fluorescence-based single-molecule PK-resistance assay. The single-molecule resolution

[1]Department of Electrical and Computer Engineering, Iowa State University, Ames, IA 50011, USA. [2]Iowa Center for Advanced Neurotoxicology, Department of Biomedical Sciences, College of Veterinary Medicine, Iowa State University, Ames, IA 50011, USA. [3]Department of Physics and Astronomy, Iowa State University, Ames, IA 50011, USA. *Corresponding author. Email: sivasank@iastate.edu

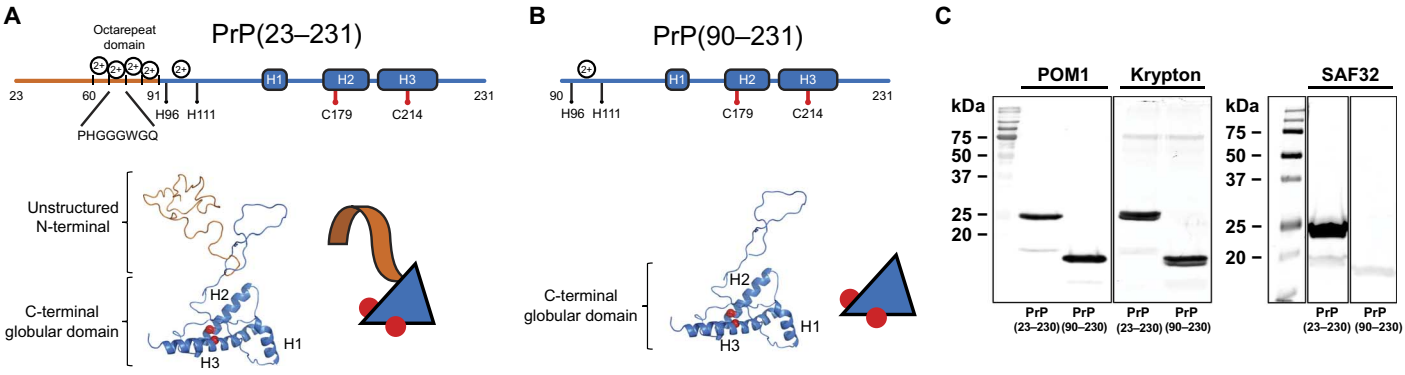

Fig. 1. PrP constructs used in the experiments. Two constructs of PrP were used in the experiments. (**A**) Full-length human PrP [PrP(23–231) or PrP(23–230)]. The unstructured N-terminal domain (orange) has four metal binding octapeptide repeats. The C-terminal domain is globular and rich in α helices (blue). Red dots indicate cysteine-179 and cysteine-214, which were used to tether PrP to the surface. (**B**) PrP without unstructured N-terminal region [PrP(90–231) or PrP(90–230)]. (**C**) SDS–polyacrylamide gel electrophoresis (SDS-PAGE) and Western blot of purified PrP(23–230) [molecular weight (MW), 25,200] and PrP(90–230) (MW, 18,500). SDS-PAGE was stained by Krypton fluorescent protein stain. The anti-prion antibodies POM1 and SAF32 were used to recognize the globular domain of PrP and the octapeptide repeats, respectively.

of our assay allowed us to measure the misfolding of PrP monomers and avoid artifacts introduced by higher-order oligomerization. In our assay, the PrPs were first biotinylated and then covalently immobilized on a glass substrate decorated with maleimide-functionalized polyethylene glycol (PEG) tethers (Materials and Methods). Surface density measurements (Materials and Methods; figs. S1 and S2) showed that the PrPs bound to the surface were well-separated monomers (table S1). The immobilized PrP monomers were incubated overnight either in the presence or in the absence of 1 mM Ni^{2+}, Mn^{2+}, or Cu^{2+} ions; dissociation constants indicate that the PrP would be saturated with the divalent ions under these experimental conditions (*11*). The samples were then treated with PK for different time periods (0 to 13 hours) and subsequently labeled with fluorescent streptavidin (Fig. 2, A to C; Materials and Methods). If the biotinylated PrP converted to a PrP^{res} conformation, it was not digested by PK and could therefore bind to fluorescent streptavidin (Fig. 2C). On the other hand, biotinylated PrP^{sen} was readily digested by PK, which resulted in a decreased binding of fluorescent streptavidin (Fig. 2, A and B). As a positive control, we covalently immobilized PK-resistant, fluorescently labeled, double-stranded DNA to identical PEG-functionalized substrates. As a negative control, PK-sensitive, biotin-conjugated bovine serum albumin (BSA) was covalently immobilized on the PEG monolayers (Materials and Methods).

Our data demonstrated that only full-length PrP [PrP(23–231)] incubated in Cu^{2+} converted to a stable PrP^{res} conformation. Even after a 10-hour exposure to PK, the fluorescence intensity of PrP(23–231) was unaltered (Fig. 2D). Similarly, the fluorescence intensity from the positive control remained unchanged after 10 hours of PK incubation. On the other hand, PK resistance was significantly reduced for PrP(23–231) bound to Mn^{2+} or Ni^{2+} and for PrP(23–231) in the absence of divalent ions; the fluorescence intensity decreased between 60 and 90% after 10 hours of PK incubation (Fig. 2D). The data in Fig. 2D were acquired from a total (summed across all time points) of 32,652, 17,638, 4776, and 29,207 PrP(23–231) molecules in the absence and in the presence of Cu^{2+}, Mn^{2+}, and Ni^{2+}, respectively.

Similarly, globular PrP that lacked the unstructured N-terminal region [PrP(90–231)] was sensitive to PK digestion in both the absence and the presence of Cu^{2+}, Mn^{2+}, and Ni^{2+}; after a 10-hour digestion with PK, the fluorescence intensity decreased between 60 and 100% (Fig. 2E). In contrast, fluorescence signal from the negative control was completely eliminated after 10 hours of PK digestion (Fig. 2, D and E). The data in Fig. 2E were acquired from a total (summed across all time points) of 9634, 12,438, 10,680, and 8869 PrP(90–231) molecules in the absence and in the presence of Cu^{2+}, Mn^{2+}, and Ni^{2+}, respectively. These results show that monomeric PrP^{res} formation requires both the intrinsically disordered N-terminal region and the Cu^{2+} ions; elimination of either results predominantly in PrP^{sen} conformation.

Full-length PrPs incubated in Cu^{2+} ions have a higher binding affinity

Next, we proceeded to use single-molecule AFM force measurements (*21*, *22*) to characterize the kinetics of the initial stage of PrP aggregation and to identify the role of different divalent metal ions and protein domains in this process. AFM–force spectroscopy (AFM-FS) has previously been used to study the misfolding and interactions of neurodegenerative proteins (*23*, *24*). Single-molecule measurements with tethered PrP monomers enabled us to directly determine association and dissociation rates while avoiding artifacts due to the formation of higher-order oligomers. Relative dimerization rates (relative on-rates) were determined from the measured binding probabilities, whereas off-rates were measured using single-molecule dynamic FS. In both sets of experiments, the PrP constructs were covalently immobilized on an AFM tip and substrate (Fig. 3, A and B; Materials and Methods) and incubated in either the presence or the absence of 1 mM Cu^{2+}, Mn^{2+}, or Ni^{2+}. The AFM tip and surface were first brought into contact, enabling opposing PrPs to dimerize. The tip was then withdrawn from the substrate and the force required to rupture the PrP dimer was recorded. If the PrPs did not interact, no unbinding forces were measured (Fig. 3C). However, dimer formation resulted in unbinding events characterized by the nonlinear stretching of the PEG tethers (Fig. 3D); the stretching of PEG served as a molecular fingerprint for PrP dimer formation because its extension under load has been extensively characterized (*25*). As described in Materials and Methods, the unbinding events were fit to an extended freely jointed chain (FJC) model (*25*) using a total least squares (TLS) fitting protocol; only unbinding events that occurred at a distance that corresponds to the contour length of two PEGs in series were used in further analysis (Materials and Methods).

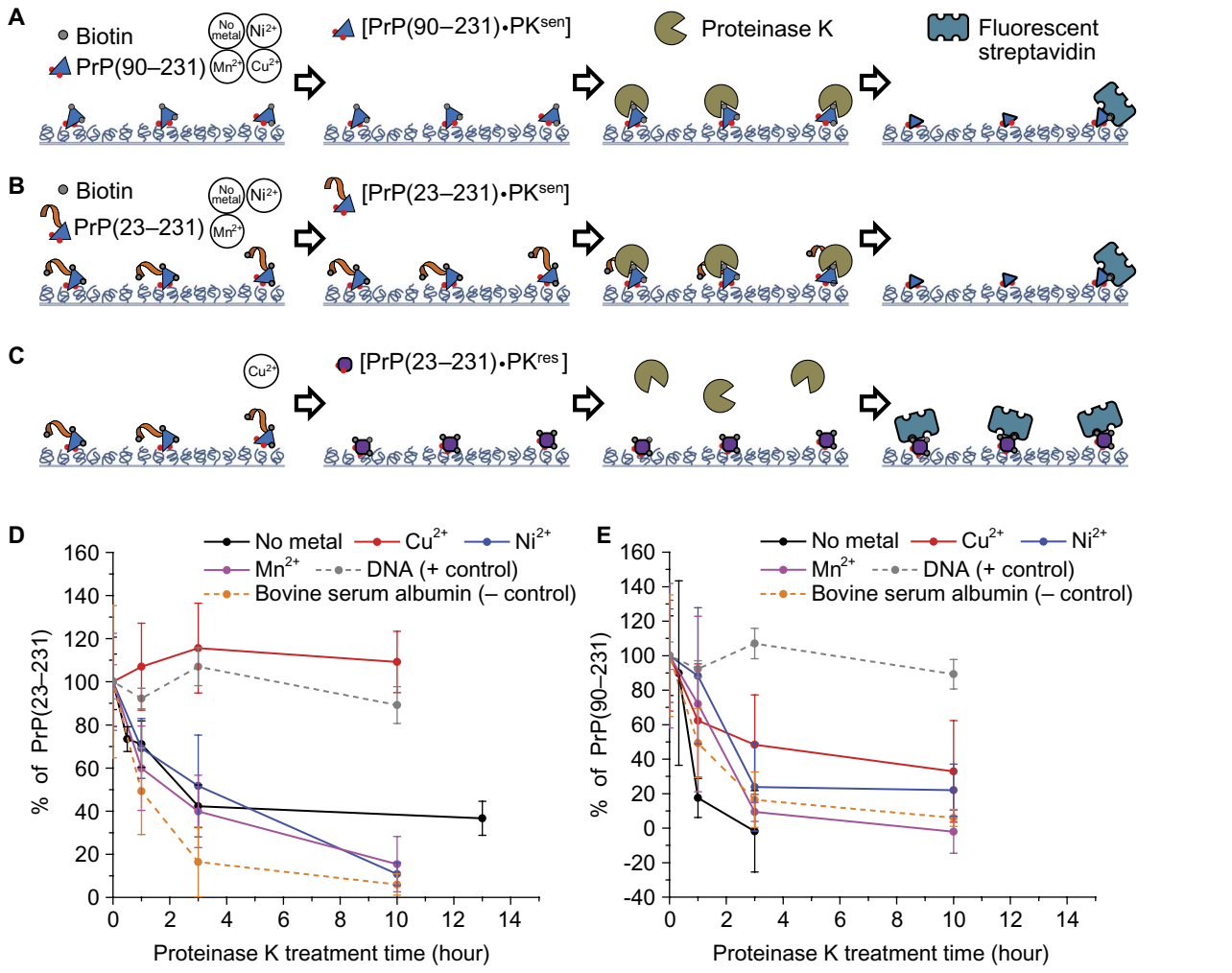

Fig. 2. Monitoring protease resistance in single PrP monomers. PrP(90–231) or PrP(23–231) was biotinylated and covalently immobilized on a substrate functionalized with a PEG monolayer. (**A** to **C**) The immobilized PrP was incubated (A) either with or without 1 mM Cu^{2+}/Mn^{2+}/Ni^{2+} [PrP(90–231)], (B) either with or without 1 mM Mn^{2+}/Ni^{2+} [PrP(23–231)], or (C) with 1mM Cu^{2+} [PrP(23–231)]. Following incubation, the immobilized PrP was digested with PK; undigested PrP was detected by labeling with fluorescent streptavidin. Structural conversion to a PK-resistant conformation resulted in a fluorescence signal. (**D** and **E**) Measured fluorescence from (D) PrP(23–231) and (E) PrP(90–231) after PK digestion for different time courses normalized by the fluorescence measured from undigested PrP under each condition. Only PrP(23–231) incubated in Cu^{2+} converted to a stable PK-resistant conformation. PEG substrates functionalized with either fluorescently labeled DNA or biotin-conjugated BSA were used as positive and negative controls, respectively. The data in (D) were acquired from a total of 32,652, 17,638, 4776, and 29,207 molecules in the absence and presence of Cu^{2+}, Mn^{2+}, and Ni^{2+}, respectively. The data in (E) were acquired from a total of 9634, 12,438, 10,680, and 8869 molecules in the absence and presence of Cu^{2+}, Mn^{2+}, and Ni^{2+}, respectively. Error bars correspond to the SE calculated using a bootstrap with replacement protocol.

Because each PrP can be tethered to the AFM tip or substrate via either one or two PEGs (covalently bound to Cys^{179} and/or Cys^{214}), we fit the unbinding events to alternate FJC models that assumed stretching of either a single tether or two parallel tethers (*26*). Our analysis showed that, in 78% of the selected events, PrP was immobilized on both the AFM tip and substrate through a single PEG tether. In contrast, 21% of unbinding corresponded to rupture events where one of the PrPs was tethered via two PEG linkers, whereas the other PrP was immobilized via a single PEG. Only 1% of the events corresponded to unbinding events where both PrPs were immobilized via two tethers. However, this heterogeneous tethering distribution did not affect the measured binding probability or unbinding force; identical results were obtained when events corresponding to the stretching of only single tethers were compared to measurements that correspond to the stretching of both single and parallel PEG tethers. The measurements were repeated several thousand times at 6 or 11 different pulling velocities and at different positions of the substrate. The surface density of PrP was estimated for every condition using single-molecule fluorescence microscopy (Materials and Methods; figs. S1 and S2); measured probabilities were normalized for direct comparison.

To identify the role of the unstructured N-terminal region in PrP interactions, we first compared the binding probability of full-length PrP(23–231) and globular PrP(90–231) in the absence of divalent metal ions. We established that our selected unbinding events had a nonspecific

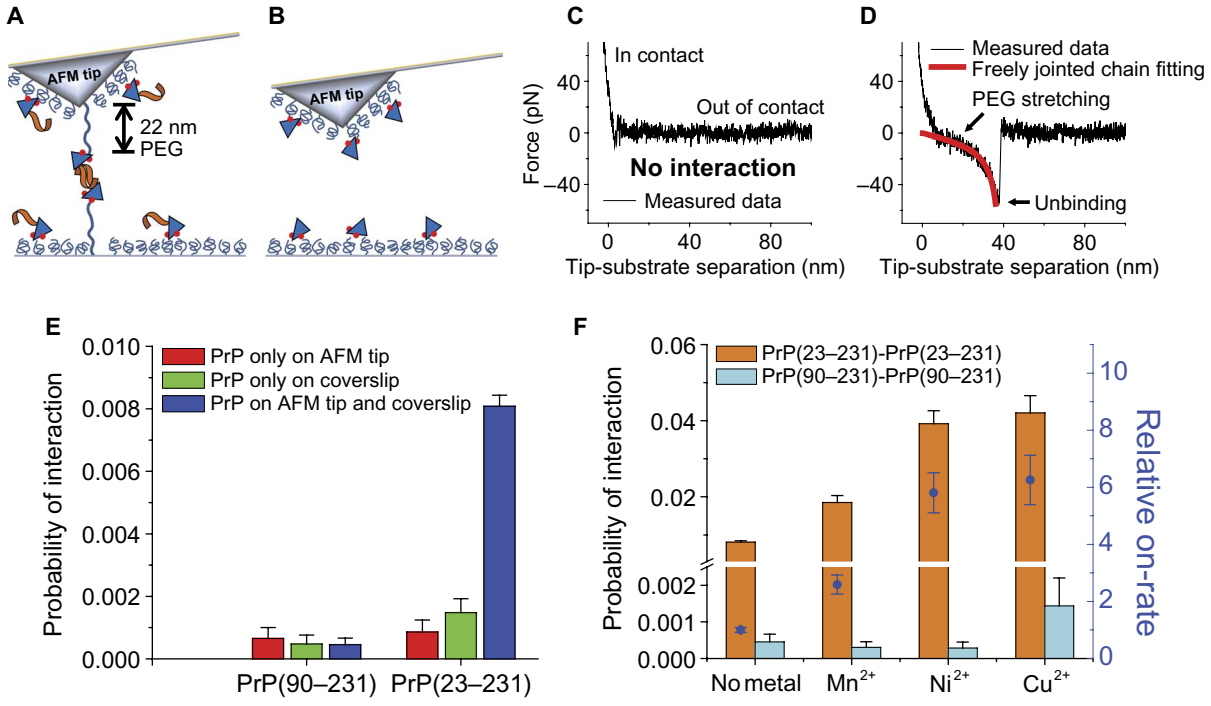

Fig. 3. Binding probabilities of full-length PrP and truncated PrP measured using single-molecule AFM. (**A** and **B**) Probability of binding was measured for (A) PrP(23–231) bound to both the AFM tip and the substrate and (B) PrP(90–231) bound to both the AFM tip and the substrate. (**C** and **D**) Representative force versus tip-substrate separation when opposing PrPs (C) do not interact or (D) interact with each other. In the case of PrP interaction, the PEG tether is stretched as an FJC before PrP unbinding. (**E**) Interaction probabilities were measured for PrP only on the AFM tip (red), for PrP only on the substrate (green), and for PrP on both the AFM tip and the substrate (blue). Red and green bars indicate the probability of nonspecific interactions. Only PrP (23–231) on both the tip and the substrate shows a higher binding rate than nonspecific interactions. (**F**) Binding probability (orange) and relative on-rate (blue) between opposing PrP(23–231) and binding probability (cyan) between opposing PrP(90–231) in the absence and presence of 1 mM Mn^{2+}, 1 mM Ni^{2+}, and 1 mM Cu^{2+}. The total number of PrP(23–231) measurements was 62,523, 20,440, 24,315, and 19,070 in the absence of divalent metal ions and in the presence of Mn^{2+}, Ni^{2+}, and Cu^{2+}, respectively. The total number of PrP(90–231) measurements was 22,048, 18,866, 8293, and 8368 in the absence of divalent metal ions and in the presence of Mn^{2+}, Ni^{2+}, and Cu^{2+}, respectively. Error bars of binding probability indicate the SE and were estimated using a bootstrap with replacement protocol. Error bars of relative on-rates indicate the SE and were propagated from the SE of binding probability.

binding probability of 0.15 ± 0.04% by eliminating PrP from either the tip or the substrate (Fig. 3E). A comparable binding probability of 0.05 ± 0.02% was measured for opposing PrP(90–231), suggesting that globular PrPs lacking the N-terminal domain do not form dimers (Fig. 3E). In contrast, PrP(23–231) dimerized with a fivefold higher probability (0.81 ± 0.04%), showing that the N-terminal tail plays a role in dimerization (Fig. 3E).

Next, we quantified the effect of divalent ions on the homotypic binding probabilities between opposing PrP(23–231) (Fig. 3A) and between opposing PrP(90–231) (Fig. 3B). Homotypic PrP(90–231) binding probabilities were comparable to nonspecific adhesion; interaction frequencies in the presence of Mn^{2+}, Ni^{2+}, and Cu^{2+} and in the absence of divalent ions were 0.03 ± 0.02%, 0.03 ± 0.02%, 0.14 ± 0.08%, and 0.05 ± 0.02%, respectively (Fig. 3F). However, homotypic PrP(23–231) binding probability was significantly enhanced by the presence of divalent ions. Although a binding probability of 0.81 ± 0.04% was measured in the absence of divalent ions, the interaction frequencies increased to 1.85 ± 0.18%, 3.92 ± 0.34%, and 4.21 ± 0.45% when Mn^{2+}, Ni^{2+}, and Cu^{2+}, respectively, were added to solution (Fig. 3F).

On the basis of the probabilities of interaction, we calculated the relative on-rates for PrP(23–231) interactions (table S2) (*27*). Because the association rates depend on factors besides microscopic binding rates, such as protein surface density, the local geometry of the tip and substrate, and the location of the proteins, all rates were calculated relative to the association rate of homotypic PrP(23–231) interactions in the absence of divalent ions (Materials and Methods) (*27*). The on-rate of homotypic PrP(23–231) was increased 6.3 ± 0.9 times in 1 mM Cu^{2+}, 5.8 ± 0.7 times in 1 mM Ni^{2+}, and 2.6 ± 0.3 times in 1 mM Mn^{2+} (Fig. 3F and table S2).

Next, using PrP(23–231), we calculated the dissociation rate by measuring the most probable rupture force at different rates of application of force; the data were fitted to the Bell-Evans equation (*28*) to extract the intrinsic off-rate (k_{off}) and the width of the potential energy barrier (x_β) that inhibits dimer dissociation (Fig. 4 and figs. S3 to S6; Materials and Methods). Our data show that PrP dimer off-rates in the absence of divalent ions and in the presence of Mn^{2+} and Ni^{2+} were comparable; the measured off-rates corresponded to 3.1×10^{-2}, 1.3×10^{-2}, and 1.0×10^{-2} s^{-1}, respectively (Fig. 4, A to C, and table S2). In contrast, the measured off-rate in Cu^{2+} was two orders of magnitude smaller with a value of 2.2×10^{-4} s^{-1} (Fig. 4D and table S2). This indicates that dimers of PrP in Cu^{2+} have lifetimes that are around 100 times longer than those of PrP^{sen} dimers.

Using the measured off-rates and the relative on-rates determined from the binding probabilities, we calculated the relative association

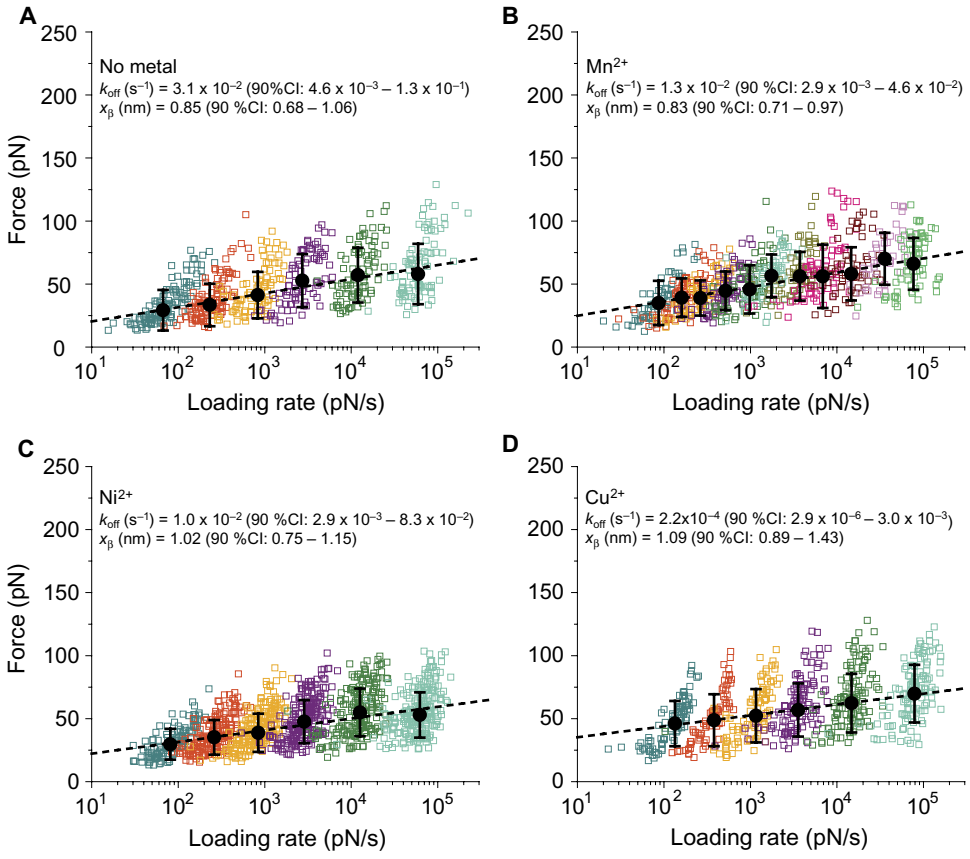

Fig. 4. Dissociation rate of PrP(23–231) dimers measured using single-molecule dynamic FS. (**A**) Plots of the measured rupture forces and loading rates in the absence of divalent ions. Colored open squares correspond to individual unbinding events at different loading rates (556 events). Black circles representing the most probable rupture forces were fit to the Bell-Evans model (black dashed line) to determine the off-rates (k_{off}) and energy barrier width (x_β). Error bars indicate the SD of forces. Ninety percent confidence interval was calculated using a bootstrap with replacement protocol. (**B** to **D**) Similar analysis for PrP(23–231) in (B) 1 mM Mn^{2+} (709 events), (C) 1 mM Ni^{2+} (1133 events), and (D) 1 mM Cu^{2+} (606 events).

constant (K_A) for PrP(23–231) in the presence of different metal ions (Materials and Methods). The K_A of PrP incubated in Cu^{2+}, Ni^{2+}, and Mn^{2+} was 863, 18, and 6 times higher, respectively, than that of PrP in the absence of divalent ions (table S2).

PrPs incubated in Cu^{2+} serve as seeds for templated aggregation

Next, we used RT-QuIC (*17*), an in vitro seeding assay, to test whether PrPs exposed to divalent metal ions form seeds that template aggregation. In a conventional RT-QuIC assay, trace amounts of scrapie seeds are added to a recombinant PrP substrate and repeatedly agitated (*17*); amyloid fiber formation is monitored through an increase in fluorescence intensity when thioflavin T (ThT) binds to the aggregate. If the seeds are active, a more rapid onset of aggregation is measured with increasing seed concentration. In our measurements, we generated PrP seeds by incubating human recombinant PrP(23–230) or PrP(90–230) in either the presence or the absence of 10 μM Mn^{2+}, Ni^{2+}, or Cu^{2+} ions at 37°C. As the PrPs began to misfold to form seeds, their aggregation was monitored using ThT fluorescence intensity; seed formation was accelerated by periodically agitating the solution (Materials and Methods). PrP(23–230) incubated in Mn^{2+}, Ni^{2+}, and Cu^{2+} ions began forming seeds between 15 and 25 hours, whereas PrP(23–230), in the absence of divalent ions, began forming seeds only after 55 hours (fig. S7). When PrP(90–230) was incubated in the presence of Ni^{2+} and Cu^{2+} ions for 95 hours, no seed formation was measured (fig. S8). However, PrP(90–230) incubated in Mn^{2+} ions began forming seeds after 85 hours (fig. S8).

We used the PrP(23–230) seeds to template aggregation of recombinant human PrP(23–230) in the absence of metal ions (Materials and Methods). Because the presence of trace amounts of divalent ions may affect in vitro conversion (*29*), 1 mM EDTA, a metal ion chelator, was included in the assay (Materials and Methods). When seeds were added to the substrate of natively folded PrP, a lag phase (T_{th}) preceded the onset of aggregation (Fig. 5A). The duration of T_{th} indicated the efficiency of the seeding reaction (*30*, *31*); for the same concentration of seeds, a shorter T_{th} indicated an earlier onset of aggregation and more efficient seed propagation. Previous theoretical studies of templated protein aggregation predict that the T_{th} depends on the amount of initial seed; a decrease in T_{th} is predicted as the seed concentration increases (Fig. 5B) (*30*). We therefore measured T_{th} when 150 fg, 1.5 pg, 15 pg, 150 pg, and 1.5 ng of seeds were added to 15 μg of recombinant human PrP(23–230) (Fig. 5, C to F, and figs. S9 to S11; Materials and Methods). Only PrP(23–230) seeds prepared in 10 μM Cu^{2+} ions showed a decrease in T_{th} with increasing seed concentration (one-tailed

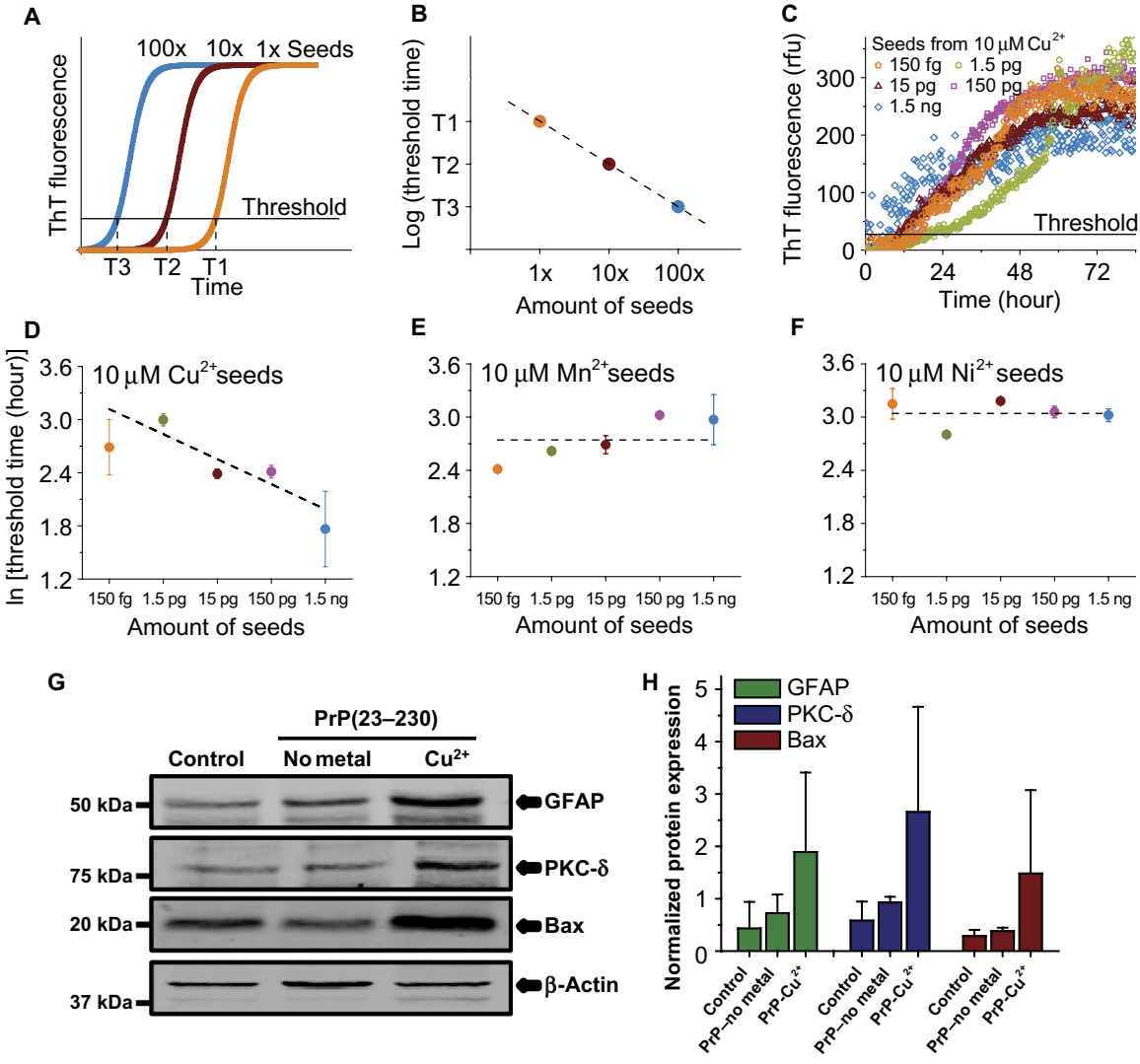

Fig. 5. Seeding activity and neurotoxicity of PrP(23–230) measured using RT-QuIC and organotypic slice cultures. (**A**) In the RT-QuIC assay, enhancement of ThT fluorescence is measured upon binding to amyloid fibrils. For nucleated polymerization, duration of the T_{th} increases when the initial amount of seeds decreases. (**B**) For templated aggregation, the duration of the T_{th} is predicted to be inversely correlated to the seed concentration. (**C**) RT-QuIC traces for 15 μg of human recombinant PrP(23–230) substrate seeded with PrP(23–230) that had been pre-exposed to 10 μM Cu^{2+}. Fluorescence signals from PrP aggregates were averaged across five replicates and were baseline-corrected. Duration of the T_{th} was determined to be the time point where ThT fluorescence intensity first increased beyond a predetermined threshold (five times the SD of blank samples without PrP seeds and substrate). rfu, relative fluorescence units. (**D**) Log-log plot of T_{th} duration for different amounts of PrP(23–230) seeds formed in 10 μM Cu^{2+}. The linear decrease in T_{th} duration with increasing seed concentration is suggestive of an inverse correlation as predicted by theory. (**E** and **F**) Similar analysis using seeds formed in (E) 10 μM Mn^{2+} and (F) 10 μM Ni^{2+} ions. In contrast to seeds formed in 10 μM Cu^{2+}, the threshold time does not decrease with increasing seed concentration, indicating that aggregation in (E) and (F) is not templated. Error bars correspond to the SE of the mean. (**G**) Representative Western blot of protein markers for neuroinflammation and neurodegeneration after organotypic slice cultures were exposed to PrP(23–230) seeds. (**H**) Quantification of Western blot band intensities shows increased GFAP, PKC-δ, and Bax protein expression upon exposure to copper-induced prion amyloids. Each group is represented by the mean ± SEM from at least four separate measurements.

t test; $P = 0.05$), suggesting an inverse correlation as predicted by theory (Fig. 5D). Similarly, when PrP(23–230) seeds prepared in 1 μM Cu^{2+} ions were used in the experiments, a more rapid onset of aggregation with increasing seed concentration was measured (fig. S12). In contrast, a decrease in T_{th} with increasing seed concentration was not observed when seeds were prepared in Mn^{2+} and Ni^{2+} ions (one-tailed *t* test; $P = 1$ and 0.81, respectively) (Fig. 5, E and F). These results demonstrate that only PrP(23–230) exposed to Cu^{2+} ions serve as seeds for the formation of PrP aggregates.

PrPs incubated in Cu^{2+} induce neuroinflammation and neurodegeneration in brain tissue

Finally, we demonstrated the cytotoxic nature of Cu^{2+}-induced PrP amyloids using a mouse organotypic slice culture assay. Slices of

brain tissue from young mice were incubated with either misfolded PrP(23–230) prepared by pre-exposure to Cu^{2+} ions (PrP-Cu^{2+}) or PrP(23–230) monomers that were not pre-exposed to Cu^{2+} (PrP–no metal). PrP-Cu^{2+} and PrP–no metal were prepared using a protocol identical to that of the RT-QuIC assay but without adding ThT (Materials and Methods). At the end of the treatment period, whole-cell lysates were prepared from the brain slices, and three protein markers for neuroinflammation and neurodegeneration were assayed using Western blot analysis (Materials and Methods). We first characterized the levels of glial fibrillary acidic protein (GFAP), an important indicator of astrocytic activation during neuroinflammation. Western blot analysis indicated that PrP-Cu^{2+} results in higher GFAP immunoreactivity than PrP–no metal or control slices that were not exposed to PrP (Fig. 5, G and H). Next, because elevated gliosis enhances oxidative stress and downstream neuronal degeneration, we also analyzed the expression of protein kinase C–δ (PKC-δ), a key oxidative stress–sensitive kinase of the novel PKC family. Activation of PKC-δ has been shown to induce neuronal cell death, and its relevance to oxidative stress–mediated neurodegeneration is seen in many neurodegenerative diseases including Alzheimer's disease, Parkinson's disease, and prion diseases (*32*–*35*). We observed significantly increased levels of PKC-δ when brain slices were incubated with PrP-Cu^{2+}. Finally, because PKC-δ is a proapoptotic kinase, its activation results in a downstream apoptotic protein cascade and neuronal degeneration. We therefore investigated the activation of one such proapoptotic protein, Bax. Our Western blot analysis showed an increase in Bax activity in mouse brain slices incubated with PrP-Cu^{2+}. We ruled out any role of the minuscule amounts of Cu^{2+} ions, which are introduced into the slice cultures upon addition of protein seeds, in enhancing these protein markers (fig. S13). Together, the notable increase in the levels of GFAP, PKC-δ, and Bax upon addition of PrP-Cu^{2+} suggests that Cu^{2+}-induced misfolding contributes to neurotoxic signaling and mediates neuronal cell death (Fig. 5, G and H).

DISCUSSION

Because PK degrades accessible regions of proteins that have flexible secondary structures, proteolytic digestion is routinely used to identify PrP domains that have misfolded into a β sheet–rich conformation. We therefore developed a fluorescence assay with single-molecule sensitivity to measure the PK resistance and, consequently, the misfolding of PrP monomers. Our experiments demonstrate that the unstructured N-terminal region and Cu^{2+} ions mediate PrP monomer misfolding and PK resistance. It has been reported that Cu^{2+} binding reduces the folding stability of PrP, making a conformation transition more thermodynamically favorable (*36*). Ensemble biophysical experiments with PrP(23–231) show that exposure to Cu^{2+} ions results in a PK-resistant conformation and that PrP^{sen} isoforms are observed in Zn^{2+}, Mg^{2+}, Ca^{2+}, Mn^{2+}, and Fe^{2+} (*12*). In contrast, PrP(90–231) forms oligomeric aggregates rich in β sheets only at acidic pH (*37*).

It has been suggested that the direct inhibition of PK by copper may be responsible for previous reports of Cu^{2+}-induced PK resistance in ensemble biochemical experiments (*38*). However, in our experiments, the Cu^{2+} ions are washed out of solution before PK incubation. Thus, our fluorescence experiments demonstrate that Cu^{2+} promotes PK resistance through direct interaction with PrP(23–231) and not by inhibiting PK itself. Furthermore, we show that PrP(90–231) exposed to Cu^{2+} remains more PK-sensitive, confirming that the Cu^{2+} ions do not inhibit PK activity. Previous studies show that PK degrades the N-terminal region of scrapie PrP without compromising pathogenicity (*39*, *40*). Experiments with transgenic mice also show that globular PrP is sufficient for propagating scrapie in vivo (*41*). In contrast, both our single-molecule and RT-QuIC data show that the N-terminal region is essential for Cu^{2+}- induced misfolding and aggregation in vitro. One possible explanation for this inconsistency is that Cu^{2+} ions trigger PrP(23–231) monomers to misfold into a distinct, noninfective strain that resists PK digestion (*42*).

In solution, unmodified PrP^{sen} and PrP^{sen} tagged with biotin and PEG tethers are equally sensitive to digestion by PK. We demonstrated this by using PK to digest unlabeled PrP(23–230), biotin/PEG-labeled PrP(23–230), unlabeled PrP(90–230), and biotin/PEG-labeled PrP(90–230) in solution (fig. S14). However, because the PrPs are tethered to a surface in our single-molecule protease resistance assay, biotinylated fragments of the digested PrP that remain immobilized following PK treatment likely account for the 40% fluorescence background measured when PrP^{sen} is digested with PK for 10 hours. A candidate biotinylated fragment is the region of PrP containing three biotinylation sites (Lys^{185}, Lys^{194}, and Lys^{204}) that lies in between the two Cys tether points. However, because the tethered fragments are expected to contribute a similar fluorescence background signal when PrP^{res} is digested with PK, this isoform is at least 60% more PK-resistant than PrP^{sen}. Our hypothesis on the origin of the background signal is supported by the complete elimination of fluorescence signal measured in the negative control (biotinylated BSA), which lacks tethered, biotinylated peptide fragments (Fig. 2, D and E).

By comparing the interaction probabilities of PrP(23–231) and PrP(90–231), we show that the unstructured N-terminal tail has a dominant influence on the first stage of oligomerization, that is, PrP dimerization. Our data suggest that in the absence of the N-terminal tail, PrP(90–231) does not dimerize within the 100-ms time window that the AFM tip and surface are held in contact. It has previously been suggested that one of the key functions of the unstructured N-terminal region is enhancing the efficiency of aggregation (*43*). This effect may be mediated by the polybasic region (residues 23 to 31) in the disordered N-terminal region, which is believed to be involved in PrP propagation (*44*). Our data also indicate that the relative association constant of full-length PrP incubated with Cu^{2+} ions was 863 times higher than the affinity in the absence of divalent ions. This increase in relative K_A could arise from a Cu^{2+}-induced tertiary structural conversion of PrP(23–231) (*45*).

In our single-molecule force and fluorescence assay, PrPs were immobilized by reducing the intramolecular disulfide bond between Cys^{179} and Cys^{214} and functionalizing the Cys residues with PEG tethers. Because tagging the Cys residues with PEG tethers can potentially destabilize PrP and promote misfolding, we used nuclear magnetic resonance (NMR) spectroscopy, dynamic light scattering, circular dichroism (CD) spectroscopy, and thermal denaturation experiments to confirm that PrP molecules are in a stable, native, monomeric conformation upon functionalization. We confirmed that the PrPs remained in their native conformation following disulfide bond reduction and PEG labeling using CD spectroscopy (Supplementary Materials; fig. S15) and ^{1}H-NMR (Supplementary Materials; figs. S16 to S23). Our CD data show that native, reduced, and PEG-functionalized PrP(23–230) and PrP(90–230) retain an α-helical content that is characteristic of natively folded PrP (fig. S15) (*46*). The α-helical content of PrP(23–230)

changed from 28 to 27%, whereas the α-helical content of PrP(90–230) changed from 43 to 35%, upon reduction of the disulfide bond. Similarly, the α-helical content of PrP(23–230) and PrP(90–230) bound to PEG is 21 and 32%. In contrast, previous CD measurements show that misfolded PrP is typically characterized by a low α-helical content of ~7% (*47*). We also used ^{1}H-NMR to confirm that the native structure of PrP(23–230) and PrP(90–230) was preserved when the disulfide bond between Cys^{179} and Cys^{214} was reduced (figs. S20 and S21) and when PrP(23–230) and PrP(90–230) were functionalized with PEG linkers (figs. S22 and S23); the chemical shift dispersions of all these structures were similar to natively folded PrP.

Furthermore, by monitoring temperature-induced unfolding of PrP(23–230) and PrP(90–230) before and after attaching PEG tethers, we confirmed that PEG functionalization does not alter the stability of the folded PrP (fig. S24) (*48*). Identical CD thermal denaturation curves with melting temperatures of 61.4° ± 0.4°C and 62.9° ± 0.7°C were measured for PrP(23–230) before and after PEG functionalization (fig. S24A). Similarly, the melting temperatures (65.1° ± 0.4°C and 65.9° ± 0.8°C) of PrP(90–230) before and after attaching PEG tethers were similar (fig. S24B). Finally, light scattering data showed that although 100% of PrP(23–230) and 96% of PrP(90–230) with intact disulfide bonds existed as monomers, reducing this linkage and functionalizing the Cys residues with PEG linkers do not significantly decrease the fraction of monomers (Supplementary Materials; fig. S25). In agreement with our results, previous studies show that reducing the disulfide bond between Cys^{179} and Cys^{214} does not alter the pathway for PrP misfolding (*49*) and that misfolding occurs without disulfide exchange (*50*).

Because previous studies have shown that aging of PrP promotes oligomerization and copper-induced PK resistance (*12*), we used PrP(23–230) and PrP(90–230) within 1 month after purification. Furthermore, we used CD and dynamic light scattering to confirm that the proteins retained their native conformation and remained in a monomeric state, even after 2 months of storage (Supplementary Materials; figs. S26 and S27). After a 2-month storage period, 96% of PrP(23–230) and 95% of PrP(90–230) remained monomeric (fig. S26), with α-helical contents of 38 and 33%, respectively (fig. S27). Because the presence of even trace amounts of misfolded PrP will result in spontaneous aggregation in an RT-QuIC experiment, the absence of large deviations between replicates (figs. S9 to S11) confirms that the PrP substrate used in our experiments is in a native conformation.

We also confirmed that the presence of an N-terminal His tag does not promote PrP denaturation or aggregation by using CD and dynamic light scattering (Supplementary Materials; figs. S26 and S27). After His tag cleavage, 92% of PrP(23–230) and 97% of PrP(90–230) remained in a monomeric state (fig. S26) and had α-helical contents of 43% (fig. S27). Finally, it is important to note that the Cu^{2+} ion–induced structural conversion of full-length PrP is not an artifact arising from the presence of His tag because the globular PrP constructs, which also contain an identical His tag, do not show Cu^{2+}-induced misfolding and aggregation.

Because the prion hypothesis proposes that misfolded seeds can template the aggregation of normal PrP into amyloid fibrils, we tested whether PrP exposed to different divalent ions can serve as seeds using RT-QuIC. Our data showed that a more rapid onset of aggregation was measured as the seed concentration increased. This correlation is predicted by theory and has previously been used to quantify the aggregation kinetics of two major forms of amyloid-β peptides (*30*, *51*).

Several studies have shown that different synthetic prion fragments promote neuroinflammatory and apoptotic responses in neuronal cells without evidence of being infectious (*52*–*54*). Therefore, to investigate the neurotoxic effect of Cu^{2+}-induced misfolded PrP, we used a mouse organotypic slice culture assay, which had been previously adopted as an excellent ex vivo model of progressive neurodegenerative disorders (*34*, *55*); a key advantage of this platform is that intact tissue explants preserve the basal cellular and molecular environment of local circuits similar to that of the whole brain. In the central nervous system, many neuropathological disorders are characteristically accompanied by activation and proliferation of glial cells that promote neuroinflammation, which is initiated relatively early in the disease process (*56*–*59*). Consistent with this, we observed an increase in the levels of the neuroinflammatory marker GFAP upon exposing brain slices to misfolded PrP. Furthermore, because oxidative stress is a critical initiator of neurotoxic insult (*32*–*35*), we analyzed the expression of the oxidative stress–sensitive kinase PKC-δ; notably, an increase in PKC-δ expression was measured when we exposed brain slice cultures to PrP amyloids. Finally, consistent with the finding that activated PKC-δ triggers the redistribution and activation of Bax, a Bcl-2 family protein that can directly induce cytochrome c release and downstream apoptotic cascade (*60*, *61*), we observed markedly increased levels of Bax in brain slices exposed to misfolded PrP. Overall, our experiments demonstrate the neurotoxicity of amyloidogenic structures resulting from PrP interaction with Cu^{2+} ions. The neuronal cell death we observed in the mouse organotypic slice culture assay directly confirms the effect of abnormal PrP, ruling out any role for the minuscule amount of Cu^{2+} ions (100 nM) in the oligomeric protein solution (fig. S13). Previous studies show that copper-induced neurotoxicity normally requires concentrations ranging from 0.1 to 1 mM in ex vivo and in vivo experimental models (*62*, *63*).

Although its physiological function is still uncertain, it has been proposed that cellular PrP plays a role in regulating Cu^{2+} homeostasis (*64*–*66*) and protecting neurons against apoptosis induced by Bax (*67*). Previous studies show that PrP is associated with Cu^{2+} ions in vivo (*9*, *68*). The average Cu^{2+} concentration in the human brain is about 80 μM (*65*), but concentrations as high as 1.3 and 0.4 mM are found in the locus coeruleus and the substantia nigra, respectively (*69*). Consequently, our experimental conditions mimic these physiological Cu^{2+} concentrations. Our data suggest that an excess of Cu^{2+} ions contributes to the structural instability and oligomerization of cellular PrP and induces neuroinflammation and neurodegeneration.

MATERIALS AND METHODS

PrP constructs used

We used recombinant, full-length, human PrP that was either purified in-house [PrP(23–230)] or purchased commercially [PrP(23–231); Jena Bioscience]. The biophysical properties of full-length PrP were compared with homegrown [PrP(90–230)] or commercially obtained [PrP(90–231); Jena Bioscience] globular PrP. ^{1}H-NMR spectra showed that the structure of PrP(23–231) and PrP(90–231) are similar to that of PrP(23–230) and PrP(90–230), respectively (Supplementary Materials; figs. S16 to S19). Plasmids for recombinant human PrP(23–230) and PrP(90–230) with an N-terminal histidine tail and an engineered thrombin cleavage site were a gift from K. Wüthrich (University of Zürich, Switzerland) (*70*). The PrP constructs were expressed and purified as previously described with minor modifications (*71*). Expression

of human PrP(23–230) and PrP(90–230) proteins was performed in *Escherichia coli* BL21(DE3) in a pRSET-A vector expression system. At an optical density at 600 nm (OD_{600}) of 0.5, PrP expression was induced with isopropyl β-D-thiogalactopyranoside (IPTG) to a final concentration of 1 mM; after 8 hours of IPTG induction, bacterial cell pellets were harvested by centrifugation. Cell lysis was carried out in 25 ml of buffer A [6 M guanidinium chloride, 10 mM tris-HCl, 100 mM Na_2HPO_4, and 10 mM reduced glutathione (pH 8.0)]. The lysate was incubated with 5 ml of Ni–nitrilotriacetic acid agarose beads (Qiagen) on a rocking shaker at room temperature for 1 hour; 5 mM imidazole for PrP(90–230) or 10 mM imidazole for PrP(23–230) was added during the incubation to prevent the nonspecific binding of protein. The resin was transferred to a column, and the beads were washed with a 200-ml gradient of buffer A to buffer B [10 mM tris-HCl and 100 mM Na_2HPO_4 (pH 8.0)] to induce PrP refolding. The column was washed with 20 ml of buffer B plus 50 mM imidazole at 4°C, and PrP was eluted with buffer C [10 mM tris-HCl, 100 mM Na_2HPO_4, and 500 mM imidazole (pH 5.8)] and dialyzed against 10 mM sodium phosphate buffer (pH 5.8). Protein concentrations were determined by a Bradford protein assay using BSA as reference. Protein fractions collected after elution were assayed for the presence and purity of PrP using SDS-PAGE with Krypton fluorescent protein staining (Pierce) and with Western blot analysis using either POM1 (Prionatis AG) or SAF32 (Cayman Chemical) (*72*, *73*) (Fig. 1C). The purified PrP was stored at 4°C and used within 1 month.

Surface and AFM tip functionalization and PrP immobilization

The protocols for functionalization of AFM cantilevers and substrates for AFM-FS experiments have been described elsewhere (*74*, *75*). Silicon nitride AFM cantilevers (Olympus) and glass substrates (Fisher) were sequentially cleaned in a solution of piranha [H_2SO_4/H_2O_2 in a 3:1 (v/v) ratio], deionized water, and acetone. The cantilevers and substrates were then silanized using a 2% (v/v) 3-aminopropyltriethoxysilane (Sigma) solution in acetone for 30 min and functionalized with a monolayer of maleimide PEG [maleimide–PEG–succinimidyl valerate; MW, 3400; Laysan Bio]. For PK digestion experiments, glass coverslips were functionalized with a mixture of 20% maleimide PEG and 80% mPEG–succinimidyl valerate (MW, 2000; Laysan Bio). Before PrP immobilization, the disulfide bond was reduced with an equal volume of 10 mM tris(2-carboxyethyl)phosphine (TCEP) for 3 hours at 4°C. The reduced PrP (23–231) or PrP(90–231), at a concentration of 1 μg/ml, was incubated on the surface in reaction buffer [50 mM sodium phosphate, 50 mM NaCl, and 10 mM EDTA (pH 7.2)] for 1 or 4 hours, respectively, at room temperature. Unlinked maleimide groups were quenched using 1 mM cysteine and 10 mM TCEP in reaction buffer overnight at 4°C.

PK digestion experiments

Biotinylation of PrP for fluorescence measurements was performed by mixing 10 mM Sulfo-NHS-LC-Biotin (Thermo Scientific) with human recombinant PrP(23–231) or PrP(90–231) (10 μg/ml) in reaction buffer for 3 hours at 4°C. The reaction was quenched by adding L-lysine (1 mg/10 μl) (Sigma) for 1 hour at room temperature. The biotinylated PrP was immobilized on PEG-functionalized glass coverslips and incubated overnight either with or without 1 mM Mn^{2+}, 1 mM Ni^{2+}, or 1 mM Cu^{2+}. Following incubation, the divalent ions were washed away, and the immobilized PrP was treated with PK (100 μg/ml) (Sigma) in buffer [25 mM tris-HCl, 5 mM $CaCl_2$, and 1 mM EDTA (pH 7.4)] for different time courses at 37°C. Following PK digestion, the PrP was labeled using Alexa Fluor 555–conjugated streptavidin (0.7 μg/ml) (Invitrogen) for 10 min at room temperature and rinsed with buffer [25 mM tris-HCl and 100 mM NaCl (pH 7.4)]. Before incubation with fluorescent streptavidin, the substrate was incubated with BSA (1 mg/ml) for 2 hours to minimize nonspecific fluorescence background. For every measurement, a blank control sample without PrP was prepared in parallel using an identical protocol. 3′-tetramethylrhodamine–modified DNA (IDT) was used as a positive control because of its resistance to PK digestion. The 5′ terminal of the DNA was modified by dithiol for surface immobilization. Biotin-conjugated BSA (Sigma), which is sensitive to PK digestion, was used as a negative control. A 50 nM solution of biotin-BSA was immobilized on maleimide PEG as described above.

For each time point, 8 to 20 fluorescence images were acquired for both the fluorescent samples and the blank control samples. We randomly selected one image each from the fluorescent and blank control data sets and recorded their difference in fluorescence intensity. This process was repeated 100,000 times. The mean and SD of these values were normalized to the intensity of an identically prepared sample without PK treatment.

Single-molecule AFM-FS

Force-ramp experiments were performed in a measurement buffer [25 mM tris-HCl and 100 mM NaCl (pH 7.4)] using an Agilent 5500 AFM system with a closed-loop scanner. The AFM tip and substrate were brought into contact for 0.1 s and then withdrawn at 6 or 11 different speeds ranging from 27 to 10,000 nm s^{-1}. Cantilever spring constants were measured using the thermal fluctuation method. Force measurements were performed continuously for 24 hours at room temperature; a LabVIEW script allowed us to operate the AFM in an automated mode to eliminate operator bias. For every experiment performed with divalent metal ions, we first acquired data for 24 hours in the measurement buffer and then acquired data for the next 24 hours in a pH 7.4 buffer with 1 mM divalent metal ions (25 mM tris-HCl, 97 mM NaCl, and 1 mM $NiCl_2/MnCl_2/CuCl_2$) to enable direct comparison. Before the experiment, the AFM cantilever and substrate functionalized with PrP were incubated in BSA (1 mg/ml) for 3 hours to minimize nonspecific protein adhesion. Each unbinding force trace was fitted to an extended FJC model (Eq. 1) (*25*), which describes the stretching of a polymer, L, under a stretching force, F

$$L = L_C \times \left(\coth\left(\frac{FL_K}{k_B T}\right) - \frac{k_B T}{FL_K} \right) + \frac{FL_C}{L_m K_s} \quad (1)$$

The model contains only one fitting parameter—the contour length of PEG tethers, L_C. The values of all other parameters were obtained from the literature (*25*). We used a value of 0.7 nm for L_K (the Kuhn length of PEG), 0.2837 nm for L_m (the average length of a PEG monomer), and 150,000 pN/nm for K_S (the stiffness of a PEG monomer). Force curves were fit using a TLS fitting protocol; goodness of fit was estimated from the residuals. For each experimental condition, the distribution of L_C from selected events was fitted to a Gaussian distribution. Only events with fitted L_C within the range of Gaussian center ± 1 SD were used to calculate the probability of interaction and off-rate.

Calculation of relative on-rates

A detailed derivation of the formulas used for the calculation of relative on-rates can be found in the study by Chesla *et al.* (*27*). Briefly, the specific binding probability was calculated as $P_{corrected} = (P_m - P_{control})/(1 - P_{control})$, where P_m is the measured binding probability when PrP is immobilized on both tip and substrate and $P_{control}$ is the measured binding probability when PrP is immobilized only on the substrate. The average number of bonds formed between opposing PrPs during each tip-substrate contact is a function of contact area between the AFM tip and substrate A_c, the protein density on opposing surfaces ρ_a and ρ_b, the contact time t, and the on-rate k_{on} and the off-rate k_{off}. Their mathematical relation is given by $\ln(1 - P_{corrected}) = A_c\rho_a\rho_b\,(1 - e^{-koff\,t})\,k_{on}/k_{off} \cong A_c\rho_a\rho_b\,t\,k_{on}$. Assuming that A_c, ρ_a, and ρ_b are fixed, the on-rate k_{on} is proportional to $-\ln(1 - P_{corrected})$.

RT-QuIC assay

PrP seeds for the RT-QuIC assay were created by incubating 6 μM PrP with 10 μM divalent metal ions ($NiCl_2$/$MnCl_2$/$CuCl_2$) in ThT assay buffer [20 mM tris-HCl, 150 mM NaCl, and 10 μM ThT (pH 7.4)]. The sample was incubated in a Cytation3 multimode microplate reader (BioTek) at 37°C for 64 to 95 hours with continuous cycles of 1-min shaking alternating with 1-min resting periods. The formation of prion seeds was detected as an increase in ThT fluorescence intensity, which was measured every 15 min. Seeds were created with three replicates for each condition. The PrP(23–230) seeds were serially diluted to a final amount of 1.5 ng, 150 pg, 15 pg, 1.5 pg, or 150 fg in 10 μl of buffer [20 mM tris-HCl and 150 mM NaCl (pH 7.4)]. Reactions were prepared in a black, 96-well, optical-bottomed plate (Nunc) with 90 μl of RT-QuIC master mix [final concentration of 20 mM tris-HCl, 150 mM NaCl, 10 μM ThT, 1 mM EDTA, and 6 μM recombinant human PrP(23–230) (pH 7.4)], and then 10 μl of seeds was loaded into wells. Sealed plates were inserted into a Cytation3 multimode microplate reader, incubated at 37°C, and shaken intermittently (1-min shake–1-min rest cycle) at 807 cpm in a double orbital configuration for 71 to 95 hours. ThT fluorescence was recorded every 15 min throughout the experiment. In each experiment, three to five replicates of blank samples [150 mM NaCl, 10 μM ThT, 1 mM EDTA, and 20 mM tris-HCl (pH 7.4)] were used. Experimental samples using seeds generated in either $NiCl_2$/$MnCl_2$ or $CuCl_2$ were examined in the RT-QuIC assay with four and five replicates, respectively. For the same seeding condition, fluorescence intensity was averaged across three to five replicates, followed by baseline subtraction and robust, locally weighted scatterplot smoothing. The duration of T_{th} was determined from the point where the ThT fluorescence intensity first reached a threshold value, where the presence of amyloid can be detected (*31*). This threshold was defined as five times the SD of the fluorescence intensity from blank samples. The SEM of T_{th} was calculated using a bootstrap with replacement protocol.

Organotypic slice culture assay and analysis

All procedures involving animal handling were approved by the Institutional Animal Care and Use Committee at Iowa State University and conducted in compliance with Association for Assessment and Accreditation of Laboratory Animal Care accreditation. Organotypic slice cultures were prepared as previously described with some modifications (*34*, *55*). Briefly, 9- to 12-day-old C57BL/6 pups were anesthetized using isoflurane, and after decapitation, brains were quickly removed and brain blocks were prepared in 2% (w/v) low–melting point agarose (Invitrogen 15517–022) in Hanks' balanced salt solution. Once the agarose was cooled on ice, 350-μm-thick cortical-striatal slices were prepared using a Compresstome VF300 microtome (Precisionary Instruments Inc.). Slices were transferred to Millicell CM Biopore PTFE membrane inserts (Millipore PICM03050) and maintained in slice culture medium (50% minimum essential medium, 25% Basal Eagle medium, 25% horse serum, and 0.65% glucose supplemented with penicillin/streptomycin and GlutaMAX) in a humidified 37°C incubator with 5% CO_2 and 95% air for 7 days. The PrP(23–230) seeds used in the organotypic assay were prepared similarly to seeds used in the RT-QuIC assay except that ThT was not used in the buffer. Seed materials were incubated and shaken using a thermomixer under the same conditions as the ThT assay either in the presence (PrP-Cu^2) or in the absence (PrP–no metal) of Cu^{2+} ions. A separate ThT assay was carried out in parallel to monitor seed formation. The formation of PrP–no metal and PrP-Cu^{2+} seeds was terminated upon observing the increase of ThT fluorescence in the ThT assay. After 1 week, organotypic slice cultures were exposed to 10 μl of the seed in 1 ml of slice culture medium for 48 hours, and 90% of the medium was exchanged every other day for another week. At the end of the treatment, slices were collected and washed with phosphate-buffered saline, and whole-cell tissue lysates were prepared using modified radioimmunoprecipitation assay buffer containing protease and phosphatase inhibitor cocktail (Thermo Scientific), as previously described (*35*, *76*–*78*). Western blot analysis on the lysates was performed using GFAP (1:2000; Millipore), Bax (1:1000; Cell Signaling), or PKC-δ (1:1000; Santa Cruz Biotechnology) antibodies. To confirm equal protein loading, blots were reprobed with β-actin (1:15,000; Sigma) antibody.

SUPPLEMENTARY MATERIALS

Supplementary material for this article is available at http://advances.sciencemag.org/cgi/content/full/2/7/e1600014/DC1

Supplementary Methods

Supplementary Results

fig. S1. Fluorescence images with different amounts of fluorescent streptavidin on the substrate.

fig. S2. Calibration plot of the number of streptavidin versus fluorescence intensity.

fig. S3. Histogram of unbinding force for PrP(23–231) measured in the absence of divalent ions.

fig. S4. Histogram of unbinding force for PrP(23–231) measured in 1 mM Mn^{2+}.

fig. S5. Histogram of unbinding force for PrP(23–231) measured in 1 mM Ni^{2+}.

fig. S6. Histogram of unbinding force for PrP(23–231) measured in 1 mM Cu^{2+}.

fig. S7. Formation of PrP(23–230) seeds monitored in real time using ThT fluorescence intensity.

fig. S8. No seeds were formed when PrP(90–230) was incubated with divalent metal ions for 84 hours.

fig. S9. Seeding activity of PrP(23–230) seeds generated in 10 μM Mn^{2+} measured using RT-QuIC.

fig. S10. Seeding activity of PrP(23–230) seeds generated in 10 μM Ni^{2+} measured using RT-QuIC.

fig. S11. Seeding activity of PrP(23–230) seeds generated in 10 μM Cu^{2+} measured using RT-QuIC.

fig. S12. Formation of PrP(23–230) seeds using 1 μM Cu^{2+} and its corresponding seeding activity.

fig. S13. Upon addition of protein seeds to brain slice cultures, residual copper does not increase levels of PKC-δ and Bax.

fig. S14. Biotinylation of PrP and functionalization with PEG tethers do not alter sensitivity to PK digestion.

fig. S15. PrP(23–230) and PrP(90–230) remain in a native conformation after reduction of disulfide bond and functionalization with PEG tethers.

fig. S16. One-dimensional ^{1}H-NMR spectra of PrP(23–231) show that the protein is in a natively folded conformation.

fig. S17. One-dimensional ^{1}H-NMR spectra of PrP(90–231) show that the protein is in a natively folded conformation.

fig. S18. One-dimensional ^{1}H-NMR spectra of PrP(23–230) show that the protein is in a natively folded conformation.

fig. S19. One-dimensional ^{1}H-NMR spectra of PrP(90–230) show that the protein is in a natively folded conformation.

fig. S20. One-dimensional ^{1}H-NMR spectra of PrP(23–230) after disulfide bond reduction show that the protein remains in a natively folded conformation.
fig. S21. One-dimensional ^{1}H-NMR spectra of PrP(90–230) after disulfide bond reduction show that the protein remains in a natively folded conformation.
fig. S22. One-dimensional ^{1}H-NMR spectra of PrP(23–230) linked to PEG tethers show that the protein remains in a natively folded conformation.
fig. S23. One-dimensional ^{1}H-NMR spectra of PrP(90–230) linked to PEG tethers show that the protein remains in a natively folded conformation.
fig. S24. Functionalization with PEG tethers does not alter the thermal stabilities of PrP(23–230) and PrP(90–230).
fig. S25. Reduction of disulfide bond and functionalization with PEG tethers do not cause aggregation of PrP(23–230) and PrP(90–230).
fig. S26. Protein age and the presence of N-terminal His tag do not cause aggregation of PrP(23–230) and PrP(90–230).
fig. S27. Protein age and the presence of N-terminal His tag do not alter the secondary structure of PrP(23–230) and PrP(90–230).
table S1. Surface density of PrP in PK digestion experiments.
table S2. Off-rate, relative on-rate, and relative association constant (K_A) for PrP(23–231) binding.

REFERENCES AND NOTES

1. M. Jucker, L. C. Walker, Self-propagation of pathogenic protein aggregates in neurodegenerative diseases. *Nature* **501**, 45–51 (2013).
2. B. Frost, M. I. Diamond, Prion-like mechanisms in neurodegenerative diseases. *Nat. Rev. Neurosci.* **11**, 155–159 (2010).
3. R. Riek, S. Hornemann, G. Wider, M. Billeter, R. Glockshuber, K. Wüthrich, NMR structure of the mouse prion protein domain PrP(121–231). *Nature* **382**, 180–182 (1996).
4. R. Zahn, A. Liu, T. Lührs, R. Riek, C. von Schroetter, F. López García, M. Billeter, L. Calzolai, G. Wider, K. Wüthrich, NMR solution structure of the human prion protein. *Proc. Natl. Acad. Sci. U.S.A.* **97**, 145–150 (2000).
5. S. Hornemann, C. Schorn, K. Wüthrich, NMR structure of the bovine prion protein isolated from healthy calf brains. *EMBO Rep.* **5**, 1159–1164 (2004).
6. D. G. Donne, J. H. Viles, D. Groth, I. Mehlhorn, T. L. James, F. E. Cohen, S. B. Prusiner, P. E. Wright, H. J. Dyson, Structure of the recombinant full-length hamster prion protein PrP(29–231): The N terminus is highly flexible. *Proc. Natl. Acad. Sci. U.S.A.* **94**, 13452–13457 (1997).
7. G. S. Jackson, I. Murray, L. L. P. Hosszu, N. Gibbs, J. P. Waltho, A. R. Clarke, J. Collinge, Location and properties of metal-binding sites on the human prion protein. *Proc. Natl. Acad. Sci. U.S.A.* **98**, 8531–8535 (2001).
8. E. D. Walter, D. J. Stevens, M. P. Visconte, G. L. Millhauser, The prion protein is a combined zinc and copper binding protein: Zn^{2+} alters the distribution of Cu^{2+} coordination modes. *J. Am. Chem. Soc.* **129**, 15440–15441 (2007).
9. D. R. Brown, K. Qin, J. W. Herms, A. Madlung, J. Manson, R. Strome, P. E. Fraser, T. Kruck, A. von Bohlen, W. Schulz-Schaeffer, A. Giese, D. Westaway, H. Kretzschmar, The cellular prion protein binds copper *in vivo*. *Nature* **390**, 684–687 (1997).
10. C. S. Burns, E. Aronoff-Spencer, G. Legname, S. B. Prusiner, W. E. Antholine, G. J. Gerfen, J. Peisach, G. L. Millhauser, Copper coordination in the full-length, recombinant prion protein. *Biochemistry* **42**, 6794–6803 (2003).
11. S. S. Leal, H. M. Botelho, C. M. Gomes, Metal ions as modulators of protein conformation and misfolding in neurodegeneration. *Coord. Chem. Rev.* **256**, 2253–2270 (2012).
12. K. Qin, D.-S. Yang, Y. Yang, M. A. Chishti, L.-J. Meng, H. A. Kretzschmar, C. M. Yip, P. E. Fraser, D. Westaway, Copper(II)-induced conformational changes and protease resistance in recombinant and cellular PrP. Effect of protein age and deamidation. *J. Biol. Chem.* **275**, 19121–19131 (2000).
13. B.-S. Wong, C. Vénien-Bryan, R. A. Williamson, D. R. Burton, P. Gambetti, M.-S. Sy, D. R. Brown, I. M. Jones, Copper refolding of prion protein. *Biochem. Biophys. Res. Commun.* **276**, 1217–1224 (2000).
14. R. A. Moore, C. Herzog, J. Errett, D. A. Kocisko, K. M. Arnold, S. F. Hayes, S. A. Priola, Octapeptide repeat insertions increase the rate of protease-resistant prion protein formation. *Protein Sci.* **15**, 609–619 (2006).
15. S. Yu, S. Yin, N. Pham, P. Wong, S.-C. Kang, R. B. Petersen, C. Li, M.-S. Sy, Ligand binding promotes prion protein aggregation—Role of the octapeptide repeats. *FEBS J.* **275**, 5564–5575 (2008).
16. B. Caughey, G. S. Baron, B. Chesebro, M. Jeffrey, Getting a grip on prions: Oligomers, amyloids, and pathological membrane interactions. *Annu. Rev. Biochem.* **78**, 177–204 (2009).
17. R. Atarashi, R. A. Moore, V. L. Sim, A. G. Hughson, D. W. Dorward, H. A. Onwubiko, S. A. Priola, B. Caughey, Ultrasensitive detection of scrapie prion protein using seeded conversion of recombinant prion protein. *Nat. Methods* **4**, 645–650 (2007).
18. J. Collinge, A. R. Clarke, A general model of prion strains and their pathogenicity. *Science* **318**, 930–936 (2007).
19. B. Oesch, D. Westaway, M. Wälchli, M. P. McKinley, S. B. H. Kent, R. Aebersold, R. A. Barry, P. Tempst, D. B. Teplow, L. E. Hood, S. B. Prusiner, C. Weissmann, A cellular gene encodes scrapie PrP 27-30 protein. *Cell* **40**, 735–746 (1985).
20. J. R. Silveira, G. J. Raymond, A. G. Hughson, R. E. Race, V. L. Sim, S. F. Hayes, B. Caughey, The most infectious prion protein particles. *Nature* **437**, 257–261 (2005).
21. E. L. Florin, V. T. Moy, H. E. Gaub, Adhesion forces between individual ligand-receptor pairs. *Science* **264**, 415–417 (1994).
22. P. Hinterdorfer, W. Baumgartner, H. J. Gruber, K. Schilcher, H. Schindler, Detection and localization of individual antibody-antigen recognition events by atomic force microscopy. *Proc. Natl. Acad. Sci. U.S.A.* **93**, 3477–3481 (1996).
23. B.-H. Kim, N. Y. Palermo, S. Lovas, T. Zaikova, J. F. W. Keana, Y. L. Lyubchenko, Single-molecule atomic force microscopy force spectroscopy study of Aβ-40 interactions. *Biochemistry* **50**, 5154–5162 (2011).
24. R. Hervás, J. Oroz, A. Galera-Prat, O. Goñi, A. Valbuena, A. M. Vera, À. Gómez-Sicilia, F. Losada-Urzáiz, V. N. Uversky, M. Menéndez, D. V. Laurents, M. Bruix, M. Carrión-Vázquez, Common features at the start of the neurodegeneration cascade. *PLOS Biol.* **10**, e1001335 (2012).
25. F. Oesterhelt, M. Rief, H. E. Gaub, Single molecule force spectroscopy by AFM indicates helical structure of poly(ethylene-glycol) in water. *New J. Phys.* **1**, 1998–1999 (1999).
26. T. A. Sulchek, R. W. Friddle, K. Langry, E. Y. Lau, H. Albrecht, T. V. Ratto, S. J. DeNardo, M. E. Colvin, A. Noy, Dynamic force spectroscopy of parallel individual Mucin1–antibody bonds. *Proc. Natl. Acad. Sci. U.S.A.* **102**, 16638–16643 (2005).
27. S. E. Chesla, P. Selvaraj, C. Zhu, Measuring two-dimensional receptor-ligand binding kinetics by micropipette. *Biophys. J.* **75**, 1553–1572 (1998).
28. E. Evans, K. Ritchie, Dynamic strength of molecular adhesion bonds. *Biophys. J.* **72**, 1541–1555 (1997).
29. O. V. Bocharova, L. Breydo, V. V. Salnikov, I. V. Baskakov, Copper(II) inhibits in vitro conversion of prion protein into amyloid fibrils. *Biochemistry* **44**, 6776–6787 (2005).
30. S. I. A. Cohen, M. Vendruscolo, M. E. Welland, C. M. Dobson, E. M. Terentjev, T. P. J. Knowles, Nucleated polymerization with secondary pathways. I. Time evolution of the principal moments. *J. Chem. Phys.* **135**, 065105 (2011).
31. D. M. Henderson, K. A. Davenport, N. J. Haley, N. D. Denkers, C. K. Mathiason, E. A. Hoover, Quantitative assessment of prion infectivity in tissues and body fluids by real-time quaking-induced conversion. *J. Gen. Virol.* **96**, 210–219 (2015).
32. M. Alfa Cissé, K. Louis, U. Braun, B. Mari, M. Leitges, B. E. Slack, A. Fisher, P. Auberger, F. Checler, B. Vincent, Isoform-specific contribution of protein kinase C to prion processing. *Mol. Cell. Neurosci.* **39**, 400–410 (2008).
33. F. Ciccocioppo, P. Lanuti, M. Marchisio, F. Gambi, E. Santavenere, L. Pierdomenico, A. Bascelli, L. Velluto, D. Gambi, S. Miscia, Expression and phosphorylation of protein kinase C isoforms in $Aβ_{1-42}$ activated T lymphocytes from Alzheimer's disease. *Int. J. Immunopathol. Pharmacol.* **21**, 23–33 (2008).
34. D. S. Harischandra, N. Kondru, D. Martin, A. Kanthasamy, H. Jin, V. Anantharam, A. G. Kanthasamy, Role of proteolytic activation of protein kinase Cδ in the pathogenesis of prion disease. *Prion* **8**, 143–153 (2014).
35. H. Jin, A. Kanthasamy, D. S. Harischandra, N. Kondru, A. Ghosh, N. Panicker, V. Anantharam, A. Rana, A. G. Kanthasamy, Histone hyperacetylation up-regulates protein kinase Cδ in dopaminergic neurons to induce cell death: Relevance to epigenetic mechanisms of neurodegeneration in Parkinson disease. *J. Biol. Chem.* **289**, 34743–34767 (2014).
36. N. D. Younan, M. Klewpatinond, P. Davies, A. V. Ruban, D. R. Brown, J. H. Viles, Copper(II)-induced secondary structure changes and reduced folding stability of the prion protein. *J. Mol. Biol.* **410**, 369–382 (2011).
37. W. Swietnicki, M. Morillas, S. G. Chen, P. Gambetti, W. K. Surewicz, Aggregation and fibrillization of the recombinant human prion protein huPrP90-231. *Biochemistry* **39**, 424–431 (2000).
38. L. A. Stone, G. S. Jackson, J. Collinge, J. D. F. Wadsworth, A. R. Clarke, Inhibition of proteinase K activity by copper(II) ions. *Biochemistry* **46**, 245–252 (2007).
39. S. B. Prusiner, D. C. Bolton, D. F. Groth, K. A. Bowman, S. P. Cochran, M. P. McKinley, Further purification and characterization of scrapie prions. *Biochemistry* **21**, 6942–6950 (1982).
40. S. B. Prusiner, D. F. Groth, D. C. Bolton, S. B. Kent, L. E. Hood, Purification and structural studies of a major scrapie prion protein. *Cell* **38**, 127–134 (1984).
41. S. Supattapone, P. Bosque, T. Muramoto, H. Wille, C. Aagaard, D. Peretz, H.-O. B. Nguyen, C. Heinrich, M. Torchia, J. Safar, F. E. Cohen, S. J. DeArmond, S. B. Prusiner, M. Scott, Prion protein of 106 residues creates an artificial transmission barrier for prion replication in transgenic mice. *Cell* **96**, 869–878 (1999).
42. E. Quaglio, R. Chiesa, D. A. Harris, Copper converts the cellular prion protein into a protease-resistant species that is distinct from scrapie isoform. *J. Biol. Chem.* **276**, 11432–11438 (2001).
43. S. Supattapone, T. Muramoto, G. Legname, I. Mehlhorn, F. E. Cohen, S. J. DeArmond, S. B. Prusiner, M. R. Scott, Identification of two prion protein regions that modify scrapie incubation time. *J. Virol.* **75**, 1408–1413 (2001).

44. J. A. Turnbaugh, U. Unterberger, P. Saá, T. Massignan, B. R. Fluharty, F. P. Bowman, M. B. Miller, S. Supattapone, E. Biasini, D. A. Harris, The N-terminal, polybasic region of PrP^C dictates the efficiency of prion propagation by binding to PrP^{Sc}. *J. Neurosci.* **32**, 8817–8830 (2012).
45. A. K. Thakur, A. K. Srivastava, V. Srinivas, K. V. R. Chary, C. M. Rao, Copper alters aggregation behavior of prion protein and induces novel interactions between its N- and C-terminal regions. *J. Biol. Chem.* **286**, 38533–38545 (2011).
46. L. Whitmore, B. A. Wallace, DICHROWEB, an online server for protein secondary structure analyses from circular dichroism spectroscopic data. *Nucleic Acids Res.* **32**, W668–W673 (2004).
47. J. C. Sang, C.-Y. Lee, F. Y. Luh, Y.-W. Huang, Y.-W. Chiang, R. P.-Y. Chen, Slow spontaneous α-to-β structural conversion in a non-denaturing neutral condition reveals the intrinsically disordered property of the disulfide-reduced recombinant mouse prion protein. *Prion* **6**, 489–497 (2012).
48. N. J. Greenfield, Using circular dichroism collected as a function of temperature to determine the thermodynamics of protein unfolding and binding interactions. *Nat. Protoc.* **1**, 2527–2535 (2006).
49. H. Yu, X. Liu, K. Neupane, A. N. Gupta, A. M. Brigley, A. Solanki, I. Sosova, M. T. Woodside, Direct observation of multiple misfolding pathways in a single prion protein molecule. *Proc. Natl. Acad. Sci. U.S.A.* **109**, 5283–5288 (2012).
50. E. Welker, L. D. Raymond, H. A. Scheraga, B. Caughey, Intramolecular *versus* intermolecular disulfide bonds in prion proteins. *J. Biol. Chem.* **277**, 33477–33481 (2002).
51. G. Meisl, X. T. Yang, E. Hellstrand, B. Frohm, J. B. Kirkegaard, S. I. A. Cohen, C. M. Dobson, S. Linse, T. P. J. Knowles, Differences in nucleation behavior underlie the contrasting aggregation kinetics of the Aβ40 and Aβ42 peptides. *Proc. Natl. Acad. Sci. U.S.A.* **111**, 9384–9389 (2014).
52. G. Forloni, N. Angeretti, R. Chiesa, E. Monzani, M. Salmona, O. Bugiani, F. Tagliavini, Neurotoxicity of a prion protein fragment. *Nature* **362**, 543–546 (1993).
53. J. Gong, A. Jellali, V. Forster, J. Mutterer, E. Dubus, W. D. Altrock, J. A. Sahel, A. Rendon, S. Picaud, The toxicity of the PrP106-126 prion peptide on cultured photoreceptors correlates with the prion protein distribution in the mammalian and human retina. *Am. J. Pathol.* **170**, 1314–1324 (2007).
54. S. Vilches, C. Vergara, O. Nicolás, G. Sanclimens, S. Merino, S. Varón, G. A. Acosta, F. Albericio, M. Royo, J. A. Del Río, R. Gavín, Neurotoxicity of prion peptides mimicking the central domain of the cellular prion protein. *PLOS One* **8**, e70881 (2013).
55. J. Falsig, A. Aguzzi, The prion organotypic slice culture assay—POSCA. *Nat. Protoc.* **3**, 555–562 (2008).
56. B. C. Gray, P. Skipp, V. M. O'Connor, V. H. Perry, Increased expression of glial fibrillary acidic protein fragments and mu-calpain activation within the hippocampus of prion-infected mice. *Biochem. Soc. Trans.* **34**, 51–54 (2006).
57. L. F. Eng, R. S. Ghirnikar, GFAP and astrogliosis. *Brain Pathol.* **4**, 229–237 (1994).
58. W. Kamphuis, C. Mamber, M. Moeton, L. Kooijman, J. A. Sluijs, A. H. Jansen, M. Verveer, L. R. de Groot, V. D. Smith, S. Rangarajan, J. J. Rodríguez, M. Orre, E. M. Hol, GFAP isoforms in adult mouse brain with a focus on neurogenic astrocytes and reactive astrogliosis in mouse models of Alzheimer disease. *PLOS One* **7**, e42823 (2012).
59. R. Kordek, P. P. Liberski, R. Yanagihara, S. Isaacson, D. C. Gajdusek, Molecular analysis of prion protein (PrP) and glial fibrillary acidic protein (GFAP) transcripts in experimental Creutzfeldt-Jakob disease in mice. *Acta Neurobiol. Exp.* **57**, 85–90 (1997).
60. S. R. Cerda, R. Mustafi, H. Little, G. Cohen, S. Khare, C. Moore, P. Majumder, M. Bissonnette, Protein kinase Cδ inhibits Caco-2 cell proliferation by selective changes in cell cycle and cell death regulators. *Oncogene* **25**, 3123–3138 (2006).
61. L. A. Sitailo, S. S. Tibudan, M. F. Denning, Bax activation and induction of apoptosis in human keratinocytes by the protein kinase Cδ catalytic domain. *J. Invest. Dermatol.* **123**, 434–443 (2004).
62. I. Paris, A. Dagnino-Subiabre, K. Marcelain, L. B. Bennett, P. Caviedes, R. Caviedes, C. O. Azar, J. Segura-Aguilar, Copper neurotoxicity is dependent on dopamine-mediated copper uptake and one-electron reduction of aminochrome in a rat substantia nigra neuronal cell line. *J. Neurochem.* **77**, 519–529 (2001).
63. A. R. White, G. Multhaup, F. Maher, S. Bellingham, J. Camakaris, H. Zheng, A. I. Bush, K. Beyreuther, C. L. Masters, R. Cappai, The Alzheimer's disease amyloid precursor protein modulates copper-induced toxicity and oxidative stress in primary neuronal cultures. *J. Neurosci.* **19**, 9170–9179 (1999).
64. E. Gaggelli, H. Kozlowski, D. Valensin, G. Valensin, Copper homeostasis and neurodegenerative disorders (Alzheimer's, prion, and Parkinson's diseases and amyotrophic lateral sclerosis). *Chem. Rev.* **106**, 1995–2044 (2006).
65. J. Stöckel, J. Safar, A. C. Wallace, F. E. Cohen, S. B. Prusiner, Prion protein selectively binds copper(II) ions. *Biochemistry* **37**, 7185–7193 (1998).
66. C. J. Choi, A. Kanthasamy, V. Anantharam, A. G. Kanthasamy, Interaction of metals with prion protein: Possible role of divalent cations in the pathogenesis of Prion diseases. *Neurotoxicology* **27**, 777–787 (2006).
67. L. Westergard, H. M. Christensen, D. A. Harris, The cellular prion protein (PrPC): Its physiological function and role in disease. *Biochim. Biophys. Acta Mol. Basis Dis.* **1772**, 629–644 (2007).
68. M. L. Kramer, H. D. Kratzin, B. Schmidt, A. Römer, O. Windl, S. Liemann, S. Hornemann, H. Kretzschmar, Prion protein binds copper within the physiological concentration range. *J. Biol. Chem.* **276**, 16711–16719 (2001).
69. I. E. Dreosti, R. M. Smith, *Neurobiology of the Trace Elements: Volume 2: Neurotoxicology and Neuropharmacology*. Contemporary Neuroscience (Humana Press, New York, 1983), pp. 1–39.
70. S. Hornemann, B. Christen, C. von Schroetter, D. R. Pérez, K. Wüthrich, Prion protein library of recombinant constructs for structural biology. *FEBS J.* **276**, 2359–2367 (2009).
71. R. Zahn, C. von Schroetter, K. Wüthrich, Human prion proteins expressed in *Escherichia coli* and purified by high-affinity column refolding. *FEBS Lett.* **417**, 400–404 (1997).
72. M. Polymenidou, R. Moos, M. Scott, C. Sigurdson, Y.-z. Shi, B. Yajima, I. Hafner-Bratkovič, R. Jerala, S. Hornemann, K. Wuthrich, A. Bellon, M. Vey, G. Garen, M. N. G. James, N. Kav, A. Aguzzi, The POM monoclonals: A comprehensive set of antibodies to non-overlapping prion protein epitopes. *PLOS One* **3**, e3872 (2008).
73. C. Féraudet, N. Morel, S. Simon, H. Volland, Y. Frobert, C. Créminon, D. Vilette, S. Lehmann, J. Grassi, Screening of 145 anti-PrP monoclonal antibodies for their capacity to inhibit PrPSc replication in infected cells. *J. Biol. Chem.* **280**, 11247–11258 (2005).
74. S. Rakshit, Y. X. Zhang, K. Manibog, O. Shafraz, S. Sivasankar, Ideal, catch, and slip bonds in cadherin adhesion. *Proc. Natl. Acad. Sci. U.S.A.* **109**, 18815–18820 (2012).
75. K. Manibog, H. Li, S. Rakshit, S. Sivasankar, Resolving the molecular mechanism of cadherin catch bond formation. *Nat. Commun.* **5**, 3941 (2014).
76. D. S. Harischandra, H. Jin, V. Anantharam, A. Kanthasamy, A. G. Kanthasamy, α-Synuclein protects against manganese neurotoxic insult during the early stages of exposure in a dopaminergic cell model of Parkinson's disease. *Toxicol. Sci.* **143**, 454–468 (2015).
77. A. G. Kanthasamy, C. Choi, H. Jin, D. S. Harischandra, V. Anantharam, A. Kanthasamy, Effect of divalent metals on the neuronal proteasomal system, prion protein ubiquitination and aggregation. *Toxicol. Lett.* **214**, 288–295 (2012).
78. A. Ghosh, H. Saminathan, A. Kanthasamy, V. Anantharam, H. Jin, G. Sondarva, D. S. Harischandra, Z. Qian, A. Rana, A. G. Kanthasamy, The peptidyl-prolyl isomerase Pin1 upregulation and proapoptotic function in dopaminergic neurons: Relevance to the pathogenesis of Parkinson disease. *J. Biol. Chem.* **288**, 21955–21971 (2013).

Acknowledgments: A.K. acknowledges the W. Eugene and Linda Lloyd Endowed Chair. We thank K.-S. Wang for advice on statistical analysis of the data and B. Fulton for technical assistance with acquisition of NMR spectra. **Funding:** This work was supported by NIH grants from the National Institute of Environmental Health Sciences (3R01ES019267 to A.K. and ViCTER grant to A.K. and S.S.). **Author contributions:** S.S. directed the research. C.-F.Y. and S.S. designed the biophysical experiments, and D.S.H. and A.K. designed the neurotoxicological assays. C.-F.Y. and D.S.H. performed the experiments and analyzed the data. S.S and C.-F.Y wrote the manuscript with assistance from A.K. and D.S.H. **Competing interests:** The authors declare that they have no competing interests. **Data and materials availability:** All data needed to evaluate the conclusions in the paper are present in the paper and/or the Supplementary Materials. Additional data related to this paper may be requested from the authors.

Submitted 5 January 2016
Accepted 27 May 2016
Published 1 July 2016
10.1126/sciadv.1600014

Citation: C.-F. Yen, D. S. Harischandra, A. Kanthasamy, S. Sivasankar, Copper-induced structural conversion templates prion protein oligomerization and neurotoxicity. *Sci. Adv.* **2**, e1600014 (2016).